3D Printed Liquid Crystal Polymer Thermosiphon for Heat Transfer under Vacuum

Seshadri, Bharath; Hischier, Illias; Masania, Kunal; Schlueter, Arno

DOI
10.1002/admt.202300403

Publication date
2023

Document Version
Final published version

Published in
Advanced Materials Technologies

ADVANCED MATERIALS TECHNOLOGIES
www.advmattechnol.de

3D Printed Liquid Crystal Polymer Thermosiphon for Heat Transfer under Vacuum

Bharath Seshadri, Illias Hischier, Kunal Masania, and Arno Schlueter*

A novel approach is presented to 3D print vacuum–tight polymer components using liquid crystal polymers (LCPs). Vacuum–tight components are essential for gas storage and passive heat transfer, but traditional polymer 3D printing methods often suffer from poor interfaces between layers and high free volume, compromising vacuum integrity. By harnessing the unique properties of LCPs, including low free volume and low melt viscosity, highly ordered domains are achieved through nematic alignment of polymer chains. Critical gas–barrier properties are demonstrated, even in thin, single–print line–walled samples ranging from 0.8 to 1.6 mm. A 200 mm evacuated thermosiphon is successfully printed, which exhibits a thermal resistance of up to 2.18 K/W and an effective thermal conductivity of up to 28 W/mK at 60 °C. These values represent a significant increase compared to the base LCP material. Furthermore, the geometric freedom, enabled by 3D printing through the fabrication of complex–shaped thermosiphons, is showcased. The authors study highlights the potential of LCPs as high–performance materials for 3D printing vacuum–tight components with intricate geometries, opening new avenues for functional design. An application of integrating 3D printed thermosiphons as selective heat transfer components in building envelopes is presented, contributing to greenhouse gas emissions mitigation in the construction sector.

1. Introduction

Over the last decade, industries ranging from building construction[1] to automobiles[2] to aerospace[3] have seen a digital transformation with the integration of 3d printing, robotic-fabrication, and assembly processes to build technologically advanced, high-performance products. Integrating 3d printing into manufacturing processes is also an opportunity to integrate heat transfer mechanisms into components, machines, and structures for thermal management. printing makes it possible to fabricate such components in a way that is impossible to realize through conventional manufacturing techniques, for example, with complex multiscale or hierarchical geometries,[4,5] tuning metamaterial characteristics[6–8] for in situ or prefabrication. Temperature-critical structures, i.e., removing and transporting heat to maintain ideal process temperatures, or maintenance-critical structures, i.e., with long lifetimes and largely unsupervised operation, are possible applications.

However, the critical performance requirements of highly efficient heat transfer components, such as evacuated heat pipes, are still challenging to achieve with 3d printing. Besides mechanical strength, high gas barrier and vacuum tightness are required for long-lasting operation. So far, researchers have 3D-printed metal components (aluminum, copper, and stainless steel) because of the high mechanical strength and gas barrier behavior. By using an energy- and resource-intensive metal sintering technique, 3D printed evacuated heat pipes for use in electronics, nuclear reactors,[9] and structurally integrated and geometrically optimized satellite systems[10] have been demonstrated.

Compared to metal 3d printing, polymer 3d printing techniques, especially fused filament fabrication (FFF), is a more cost-, material-, and energy-efficient[11] alternative. It has been shown that polymer heat pipes can achieve high heat- and mass transfer performance.[12–16] Polymer 3D printed parts can be built on top of different substrates, thus allowing heat pipes to be integrated into digital fabrication and assembly processes. However, the critical performance characteristics of heat pipes, i.e., high gas barrier and mechanical strength to maintain vacuum pressure, are more challenging to achieve compared to the metal sintering techniques. To achieve vacuum compatibility for polymer FFF 3D printed parts require considerable time- and resource-intensive postprocessing, e.g., annealing polymer-metal composites,[17] coating with a sealant or metal electroplating[18] to improve vacuum performance. Large-scale

B. Seshadri, I. Hischier, A. Schlueter
Architecture and Building Systems
ETH Zurich
Stefano Franscini Platz 1, Zurich 8093, Switzerland
E-mail: seshadri@arch.ethz.ch

K. Masania
Shaping Matter Laboratory
Faculty of Aerospace Engineering
TU Delft
Kluyverweg 1, Delft 2629 HS, The Netherlands

The ORCID identification number(s) for the author(s) of this article can be found under https://doi.org/10.1002/admt.202300403

DOI: 10.1002/admt.202300403

architectural applications, as we describe in Section 3.3, requires larger postprocessing equipment (ovens, and solution containers). Fabricating vacuum-compatible parts without postprocessing is therefore highly desired for construction.

Here we show that liquid crystal polymer (LCP) samples can be printed using an off-the-shelf 3D printer to achieve high gas-barrier properties without any postprocessing to solve the problem of hermetically sealing FFF polymer components. Coupled with optimal FFF 3D printing parameters, we demonstrate that the critical gas-barrier properties can be achieved even in thin-, single-walled (0.8–1.6 mm) components for different scales and geometries.

1.1. Material, Morphology, and Fabrication Process

The LCP (Vectra A950, Ticona) used in this research has strong mechanical properties (rupture modulus = 135–145 MPa, specific stiffness (10.6–10.9 MN m kg^{-1}), and high gas barrier (0.0184–0.0326 cm^3 mm m^{-2} day bar for O_2 gas), compared to other FFF 3D printed thermoplastics such as polypropylene (PP), acrylonitrile styrene acrylate (ASA), acrylonitrile butadiene styrene (ABS), polyethylene terephthalate glycol (PETG), polycarbonate (PC), and polyether ether ketone (PEEK). We compare these properties of commonly printed materials and LCPs in the Supporting Information S1. Among the commercially available FFF compatible 3D printed polymers, PEEK (specific stiffness 2.87–3.02 MN m kg^{-1}, flexural strength 105–116 MPa, O2 gas permeability 6.54–11.3 cm^3 Mm m^{-2} day bar) could also be used. Based on more recent information, PEI (specific stiffness 2.27–2.4 MN m kg^{-1}, flexural strength 144–159 Mpa) could be a strong alternative to LCPs for vacuum-compatible applications. The gas barrier properties should be further investigated. Noteworthy is that both PEEK and PEI require carefully controlled chamber temperatures, whereas LCPs do not and are far better suited to scaling in size, through lower energy consumption and need for specific print environment conditions.

We used a bio-inspired patented process[19] to FFF 3D print nematically aligned polymer chains in an extruded LCP filament. We used the LCP filament developed by the process of i) drying, ii) heated extrusion, iii) cooling, and iv) rolling to achieve a filament diameter of 1.75 mm which was verified using digital callipers. When extruded through a heated nozzle, the shearing stresses on the filament result in highly oriented domains. Upon exiting the nozzle, the outer domains are in contact with the ambient air, experience rapid cooling, and retain their highly ordered structure. The domains in the interior of the filament are cooled more slowly and have sufficient time to reorient, resulting in a highly oriented shell and a less-oriented core. The process combines geometric freedom with molecular orientation along the print path to achieve exceptional mechanical strength and stiffness (**Figure 1**).

We make use of the low free volume in LCP structures that have properties ideally suited for high-vacuum applications, namely high gas-barrier and mechanical properties due to the highly oriented nematic domains. The overall gas barrier of the FFF 3D printed LCP element depends on the bulk diffusion across the material (Q_{ML}) and the leakage rate between the additively deposited layers (Q_{LL}) resulting from small voids or imperfections induced during the FFF process within the printed layers. However, despite a high Q_{ML} (0.9 cm^3 m^{-2} day bar for Oxygen gas), the leakage rate between the additively deposited layers (Q_{LL}) that depends on the printing parameters and tool-path settings needs to be minimized.

2. Results and Discussion

2.1. 3D Printing Parameters and Tool-Path Settings

We identified the effect of FFF 3D printing parameters and tool-path settings on the printed sample's ability to hold vacuum. The inherent drawback of FFF 3D printed parts arises from the process itself. Since the process is "additive," small voids or imperfections are induced within the printed element, which results in air leakage or structural failure when exposed to vacuum conditions. Others have similarly investigated the impact of 3d printing parameters on performance-critical properties, mainly mechanical strength.[20–24]

Through a preliminary statistical analysis, we concluded that print temperature (T_N), nozzle size (D_N), boundary shells, or, in the case of single-walled structures—layer width (L_W) and layer heights (L_H) —were critical parameters for gas-barrier (Supporting Information S2). We first examined the effects of these parameters using optical microscopic images for imperfections that could compromise the ability to hold vacuum (**Figure 2**). Using the microscopic images, we determined boundary conditions for print temperature, layer height, and the ratio of layer width to nozzle diameter (L_W:D_N >1.0) or extrusion multiplier for single-walled structures (Figure 2C). With T_N = 330 °C, L_H = 1 mm, and L_W:D_N > 1.0, we observed better layer adhesion and a lower chance of defects. When we printed LCPs at lower temperatures (T_N < = 290 °C), we observed layer delamination, i.e., adjacent layers could not bond because of the speed at which the deposited layers were cooled. Similarly, when we printed larger layer heights (L_H > = 0.5 mm), we observed defects because of the presence of defects because of smaller contact area between adjacent layers. The images also confirm the "core–shell" structure of oriented (lighter regions) and nonoriented polymer chains (darker areas) caused by the differential cooling rates of the polymer chains, clearly visible in larger layer heights. More oriented domains have higher optical reflectivity and appear white, whereas nonoriented domains tend to have lower reflectivity and appear dark. We show a larger sample with the core–shell structure in the Supporting Information S3.

We determine that layer adhesion and, in turn, vacuum compatibility (gas-barrier and mechanical strength) can be optimized by choosing the optimal parameters. However, the extruder's vertical movement after each layer's completion and before starting the next (commonly referred to as "z-hop") results in a "z-seam" with surface defects causing voids and renders FFF samples incompatible with vacuum applications. To counter these defects, we used a continuous tool path to program the movement of the nozzle. More commonly known as the "spiral" or "vase" mode, the print layers progress upward in one continuous spiral path. Instead of countable layers, we build the sample through smooth, continuous movements of the *z*-axis (Figure 2E). We show the macro and microscopic differences between layer-upon-layer FFF 3D printed samples and samples

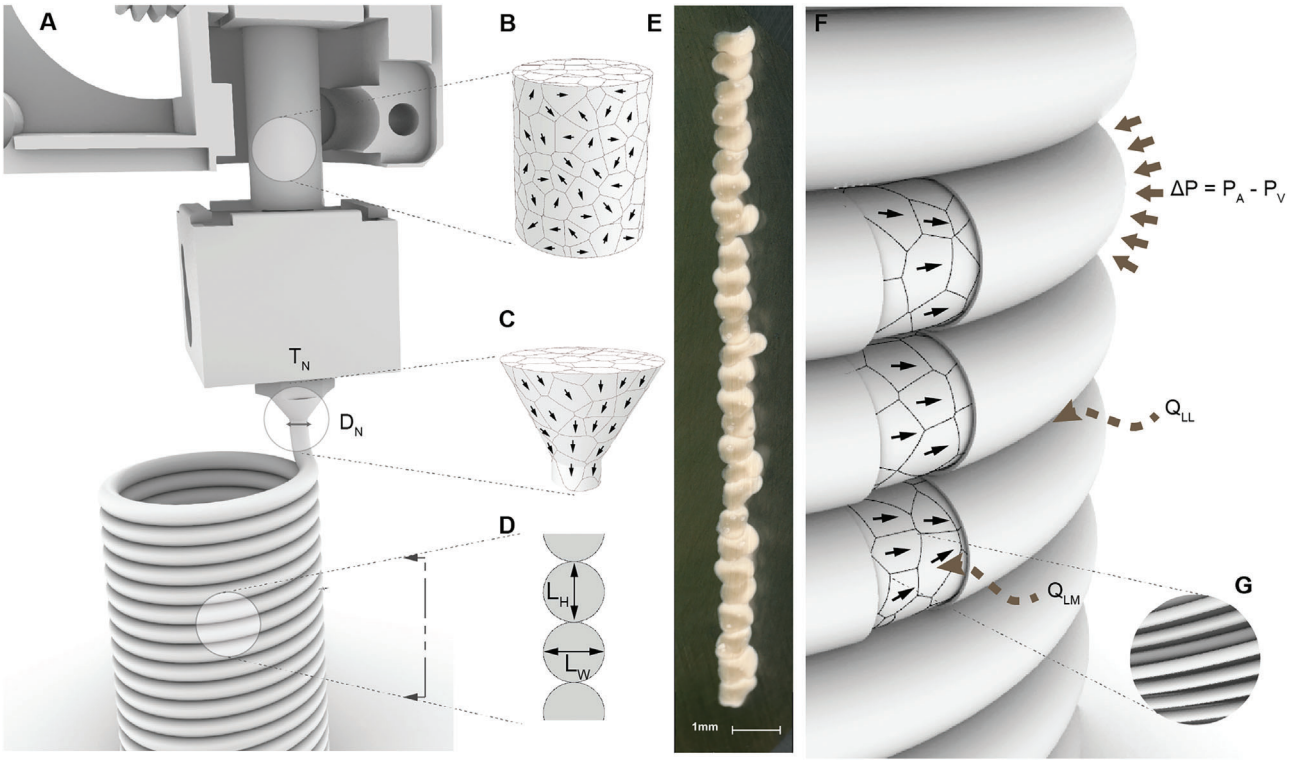

Figure 1. Schematic 3d printing process of a vacuum-tight liquid crystal polymer (LCP) cylinder showing A) FFF process and print path; polymer chain orientations within the filament, B) before- and C) after-heated extrusion. D) Cross-section of the cylinder wall describing additively deposited layers' characteristics, namely Layer Height (L_H) and Layer Width (L_W), and E) optical microscopy image of the cross-section wall demonstrating the "core–shell" morphology, i.e., light-colored shells and darker cores – indicating highly ordered shells and less-ordered cores, and F) a description of vacuum induced surface pressure (ΔP) as a result of different pressures on the inside (P_v) and outside (P_A) the component, and material- (Q_{LM}) and layer- (Q_{LL}) leakage through the walls, and G) schematic of oriented polymer chains with high gas barrier properties.

printed in a continuous spiral path in the Supporting Information S3.

Following this image analysis, we measured the effect of the above-mentioned parameters (T_N, L_H, and L_W:D_N) on the gas barrier using leak testing.

2.2. Characterizing Gas-Barrier and Leakage Rates Relative to 3D Printing Parameters

We used the insights gained from microscopic imaging to identify the FFF 3D-printing parameters necessary to fabricate samples with high gas-barrier properties. We printed single-walled, hollow cylinders (inner diameter 51.7 mm, height 100 mm) with different parameters, which could be used to quantify the gas barrier properties by measuring the samples' leakage rate.

In **Figure 3**A–C, we show the influence of print temperature, layer height, and layer width: nozzle diameter on the relative leakage rates of the samples from the leak test. Relative to the normalized baseline leakage rate at the start of the test (10^{-12} mbar L s^{-1}), at T_N = 330 °C and L_H = 0.1 mm, we found the relative leakage rate to be the lowest ($<10^{-11}$ mbar L s^{-1}) and the least spread in the measurement results. We concluded that we minimize the imperfections in layer adhesion under these conditions. At T_N> 330 °C, the LCP material exits the nozzle uncontrolled manner, which causes defects in the print. The optimized T_N and L_H parameters were used to determine the effect of L_W:D_N, tool path (spiral vs nonspiral), and postprocessing (annealing) on the relative leakage rates (Figure 3C). We increase L_W:D_N, from 1.0 to 2.0, i.e., for D_N = 0.8 mm, L_W increased from 0.8 to 1.6 mm, by increasing the amount of extruded material. We found that relative leakage rates were the smallest (10^{-12} mbar L s^{-1}) for L_W:D_N, = 2, i.e., D_N = 0.8 mm, and L_W = 1.6 mm. "Non-spiral" samples had more defects (significantly along the *z*-axis seam) and higher leakage rates than the spiral samples. Annealing (200 °C for 3 h) did not substantially affect the relative leakage rates, despite evidence that annealing leads to better layer adhesion in FFF samples.[25,26] The analysis shows that FFF 3D Printed LCP samples do not require postprocessing to achieve high gas-barrier characteristics and can meet the leakage rate requirements of vacuum applications.

Next, temporal tests were conducted to measure the absolute leakage rates for samples with optimal printing parameters. The length of the samples was increased from 100 to 200 mm to detect increase in defects/leakage rate with surface area. Components are classified as leaky if Q is $>10^{-4}$ mbar L s^{-1} and tight if $<10^{-6}$ [27] within 10 and 100 mbar. Consistent with the results from the leakage test, increasing the L_W:D_N ratio decreases the leakage rate, while increasing the length of the sample has no significant effect on the leakage rate. The leakage rates shown here could also be the result of outgassing of the sample and residual moisture build-up resulting in a higher leakage rate than

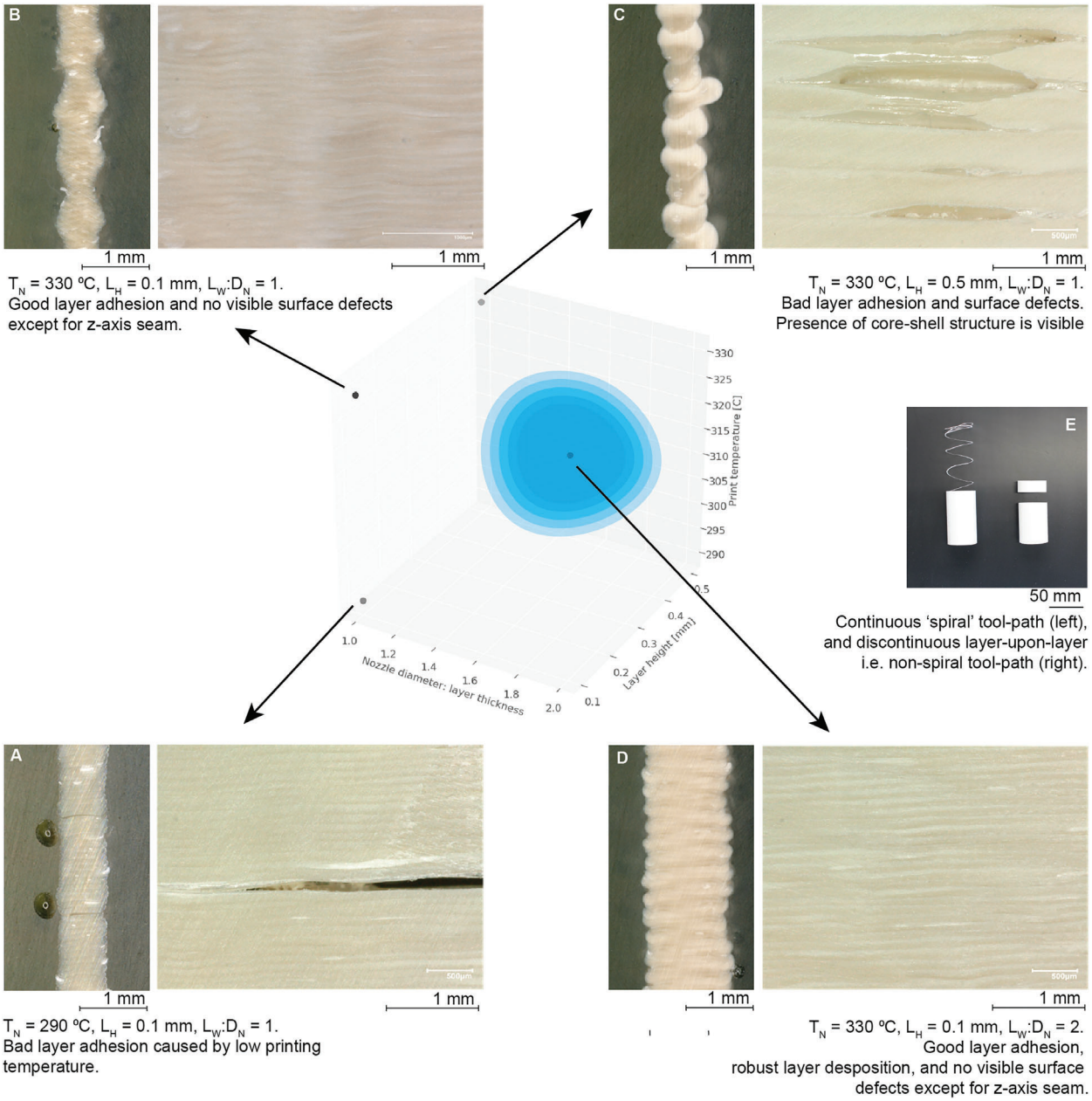

Figure 2. A–D) Polarized light microscopy of 3D printed LCP samples cross-sections (left) and side-views (right) describe the interlayer adhesion resulting from different 3d printing parameters, namely printing temperature (T_N), layer height (L_H,) and layer width to nozzle ratio (L_W:D_N). The 3D plot shows the identified 3d printing envelope that enables vacuum-tight prints. E) Images of a continuous "spiral" tool path, and a discontinuous, layer-upon-layer deposition in a "non-spiral" tool paths shown for delaminated samples.

a completely evacuated sample. In the Supporting Information S4, we demonstrate the long-term (>800 h) applicability of FFF 3D printed LCP samples by measuring the leakage behavior of a 200 mm prototype cylinder printed using the optimal print,-parameters, and path.

Our results indicated that LCPs exhibited significantly lower leakage rates with optimized printing parameters. The findings suggest that LCPs have potential for vacuum applications, but further research is needed to fully understand their gas barrier properties and compare their performance to other vacuum-compatible materials. For example, future work should include investigating the gas barrier properties of FFF polymers, such as polyetheretherketone (PEEK), polyetherimide (PEI), and a blend of PEEK/PEI. As noted in the literature, PEEK, PEI, and PEEK/PEI blends have excellent properties for space applications.[24,28–30] However, we did not find any vacuum tightness, leakage rate, or gas barrier data for 3D printed samples of these materials in the literature. Other researchers demonstrated leakage and vacuum applications of FFF polymers, but they required postprocessing using electroplating or coatings[18] to achieve a comparable results from the He leak tests, and low leakage rates (10^{-6}–10^{-8} mbar L s^{-1}) for temporal vacuum tests.

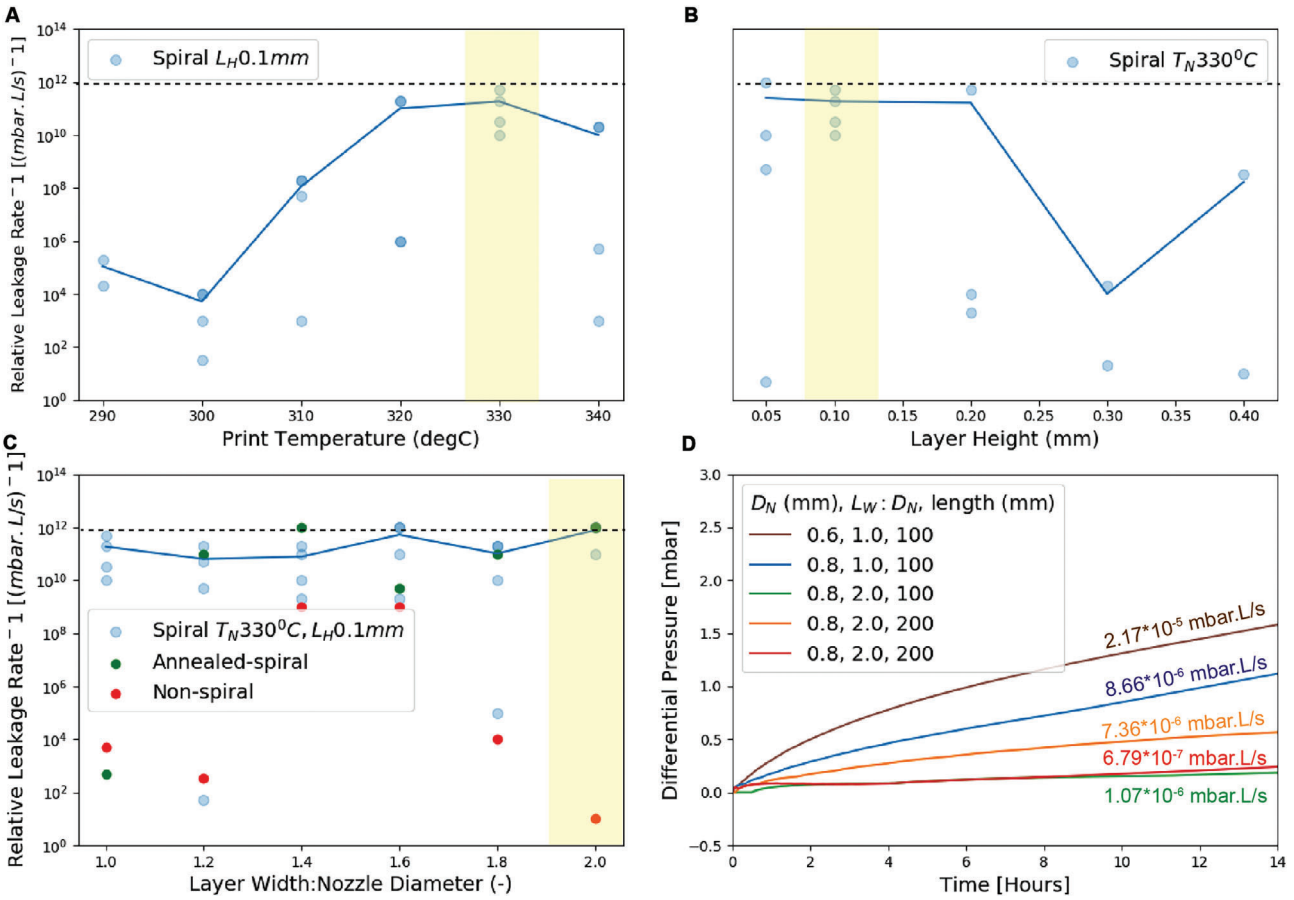

Figure 3. Analysis of the effect of critical 3d printing parameters on the leakage rates of the printed LCP samples, and identification of an optimal combination of parameters A) $T_N = 330$ °C, B) $L_H = 0.1$ mm, C) L_W:$D_N = 2$, and comparison to samples printed using nonspiral tool-paths and samples which are postannealed. The "dashed-line" shown in (A–C) are the normalized base-line vacuum pressure within the samples prior to He being sprayed. The yellow highlighted sections achieved the lowest relative leakage rates and are the optimal print parameters and path D) Short-term leakage (14 h) testing of air leakage by measuring the internal air pressure of a ∅52, 200 mm prototype printed using optimal 3d printing parameters and tool path.

The gas-barrier performance of FFF printed LCP elements is attributed to two aspects: i) the low permeability of the LCP material itself, and ii) the optimized printing parameters to reduce defects, without the use of postprocessing, which has implications for resource usage and recyclability.[17–19,31] Our contribution falls under the second aspect, where we investigated ideal printing parameters to reduce defects and maintain low permeability. Additionally, we demonstrate the effect of printing parameters on the crystalline and noncrystalline regions in Figure 2; and the Supporting Information S3. Future studies will test the layer adhesion and explore the effect of crystalline fraction of FFF printed LCP on gas barrier properties[32–34] and the use of larger extruder nozzles, which could become a critical issue. Nozzle geometry could be tweaked to achieve better adhesion and higher crystallinity, thus improving gas barrier properties.[35–37]

2.3. Performance of Prototype FFF 3D Printed LCP Thermosiphon

Using the process proposed above to achieve vacuum-tight samples, in this section, we demonstrate a prototype of an evacuated FFF 3D printed LCP thermosiphon. A thermosiphon is a type of heat pipe—a device that rapidly transfers heat from a high-temperature "source" to a low-temperature "sink" without additional mechanical action. Typically, they are hollow cylinders, partially filled with a liquid. When heat is applied, the liquid absorbs and transitions to vapor, travels along the adiabatic section(s), condenses at the cold interface(s), and releases the latent heat. The liquid returns to the hot interface either by gravitational force in the case of the thermosiphon or through the capillary action of a microporous wick in the case of a wicked heat pipe. Before usage, heat pipes are evacuated and hermetically sealed. The vacuum inside the pipe is critical to its operation and allows the working fluid to change phase at lower temperatures. Due to the high heat transfer coefficients for evaporation and condensation, heat pipes are highly effective thermal conductors (several orders of magnitude higher than the base material). Heat pipes are effective at transferring heat at high power rates over long distances with minimal heat losses. Since they contain no mechanical components, they tend to have a long lifespan with no maintenance.[38] Thermosiphons and heat pipes have been applied for heat transfer applications in buildings and infrastructure. Gaugler patented the working principle in 1944[39] as an air-conditioning system that cools the inside of a building by using

heat pipes connected to a pan of crushed ice. In 1962, engineers at the Los Alamos National Laboratory, USA, and National Aeronautics and Space Administration (NASA) installed metal heat pipes for satellites to circulate heat from the side of the satellites facing the sun to the dark side. Since then, heat pipes have been used extensively in heat-transfer applications in electronic devices, solar thermal collectors, permafrost cooling of long-distance pipelines, heat recovery for air-conditioning, nuclear reactors, and combustion engines. The benefits of using heat pipes (highly efficient, zero-energy, lightweight, highly robust) as thermal management components have been reported across several industries.[38,40,41] Researchers have determined key design parameters and operating boundary conditions of heat pipes.[42–45]

After achieving the printing of vacuum-tight FFF 3D printed LCP prototypes, we demonstrate the performance of a prototypical thermosiphon (inner diameter 51.7 mm, thickness 1.7 mm, length 200 mm). The working principle of the thermosiphon using a simple schematic and a computational fluid dynamic (CFD) simulation is described in the Supporting Information S6.

The experimental setup (**Figure 4**A) is described in the Experimental Section. For increasing input powers, an increasing temperature gradient in the evaporator section of the thermosiphon was observed, likely because of a higher evaporation rate in the upper part of the evaporator section. An increasing difference between the average evaporator ($T_{evap,avg}$) and condenser ($T_{cond,avg}$) temperatures from 2.63 to 27.41 K with increasing input power ($\dot{Q}_{in}$) from 1.0 to 14.0 W were also noted. In Figure 4C,D, the surface temperature difference was used to plot the thermal resistance (R) which decreases from 4.33 to 2.23 K W^{-1}, and effective thermal conductivity (k_{eff}) which increases from 13.30 to 25.68 W mK^{-1} for the same range of $\dot{Q}_{in}$.

The thermal conductivity was measured of the base material (3D printed LCP) using the Transient Hot Bridge (THB) method (Supporting Information S5). For the optimal FFF parameters ($T_N = 330$ °C, $L_H = 0.1$ mm, $L_W{:}D_N = 2.0$), the thermal conductivity is 0.45 W mK^{-1} with variability in the measurement direction relative to printing/layer orientation. The FFF 3D printed LCP thermosiphon has a k_{eff} between 30 and 58 times higher than the base material depending on $\dot{Q}_{in}$. Although the absolute k_{eff} is several magnitudes lower than conventional metal thermosiphons owing to the thermal conductivity of the base material, the scale factor is comparable.

In this research, we studied the effectiveness of an FFF 3D printed LCP polymer thermosiphon. Prior research in polymer thermosiphons focused on using a combination of polymer (polyvinylchloride,[12] fluororubber,[15] polyurethane,[16] and PET [14]) with metal (copper). These non-3D printed prototypes were thin (diameters ranging between 1.8 and 6 mm) and long (length ranging between 75 and 450 mm) thermosiphons. At the highest reported fill ratios (30–60%) and input powers (6–25 W), these thermosiphons achieved thermal resistances between 0.8 and 1.5 K W^{-1}, with further improvement at optimal fill-ratios. Recently, a purely TPU polymer heat-pipe[46] with a fill ratio of 60% and input power of 6 W achieved a thermal resistance of 3.5 K W^{-1}. It is worth noting that metal thermosiphons of similar length have demonstrated higher power throughput (100 W and above) compared to polymer or metal-polymer thermosiphons, with thermal resistance values below 1.5 K W^{-1}.[47] Based on these findings, the following improvements can be made to reduce the thermal resistance below 1.5 K W^{-1}: i) optimization of fill ratio and dimensions of the evaporator- and condenser-sections, ii) inclusion of metal components in the evaporator and condenser sections, and iii) increasing the heat-transfer rate in these sections through improved surface area between the wall of the thermosiphon and the working fluid.

3. Conclusions and Future Outlook

3.1. Geometrical Explorations and Applications

Several thermal management applications require passive, zero-energy removal, and transfer of heat. By fabricating thermosiphons with complex forms using 3d printing, we found that heat sources and sinks can be thermally bridged despite specific geometric requirements or spatial constraints. The design freedom increases the application of thermosiphons in new industries.

Figure 5A shows a FFF 3D printed LCP thermosiphon with a "double-curved" geometry. The evaporator section of the sample was heated to 35 °C, and observed a surface temperature difference of 4 K over 150 mm using an IR camera (FLIR E96). Unlike the linear prototypes, we did not apply insulation to observe the surface distribution better using an IR camera. Under the same conditions, a "helical" geometry shows a more uniform surface temperature (1.2 K over 150 mm) distribution. The effective thermal conductivity of thermosiphons with complex geometries depends on the barrier to vapor flow and the heat-transfer coefficients of the surface geometries. For these reasons, helical geometry performs better than double-curved geometry. We note that these samples have been printed using a commercially available 3-axis 3D printer. Samples were also prototyped with 5-axis robotic extruder to demonstrate that more complex geometries may be fabricated (Supporting Information Video S1).

3.2. Application in Energy-Efficient Architecture

In the architecture and building construction context, there is an interest in using recyclable polymers and large-scale robotic material extrusion because of their cost-, material-, and energy-efficiency.[48–51] The introduction of digital fabrication in building construction[52,53] facilitates the integration of more sophisticated, zero-energy heat transfer mechanisms within building structures. Polymers can serve as effective insulating materials, particularly when designed with higher porosity.[54,55] However, here we propose a heat transfer component by integrating a polymer-based thermosiphon within a building façade to selectively insulate and conduct heat depending on the outdoor and indoor conditions. The proposed façade would reduce the demand for building heating and cooling systems, comprising nearly half of the CO_2 emissions of global building stock (30% of global emissions)[56] while maintaining a comfortable indoor environment for occupants. Figure 5C,D shows, how we apply the research described in this paper in the FFF 3D printed LCP thermosiphon facade application. The orientation and geometry use the "helical" and "curved" geometries described in Figure 5A,B to harness the solar radiation of the winter sun to heat indoors.

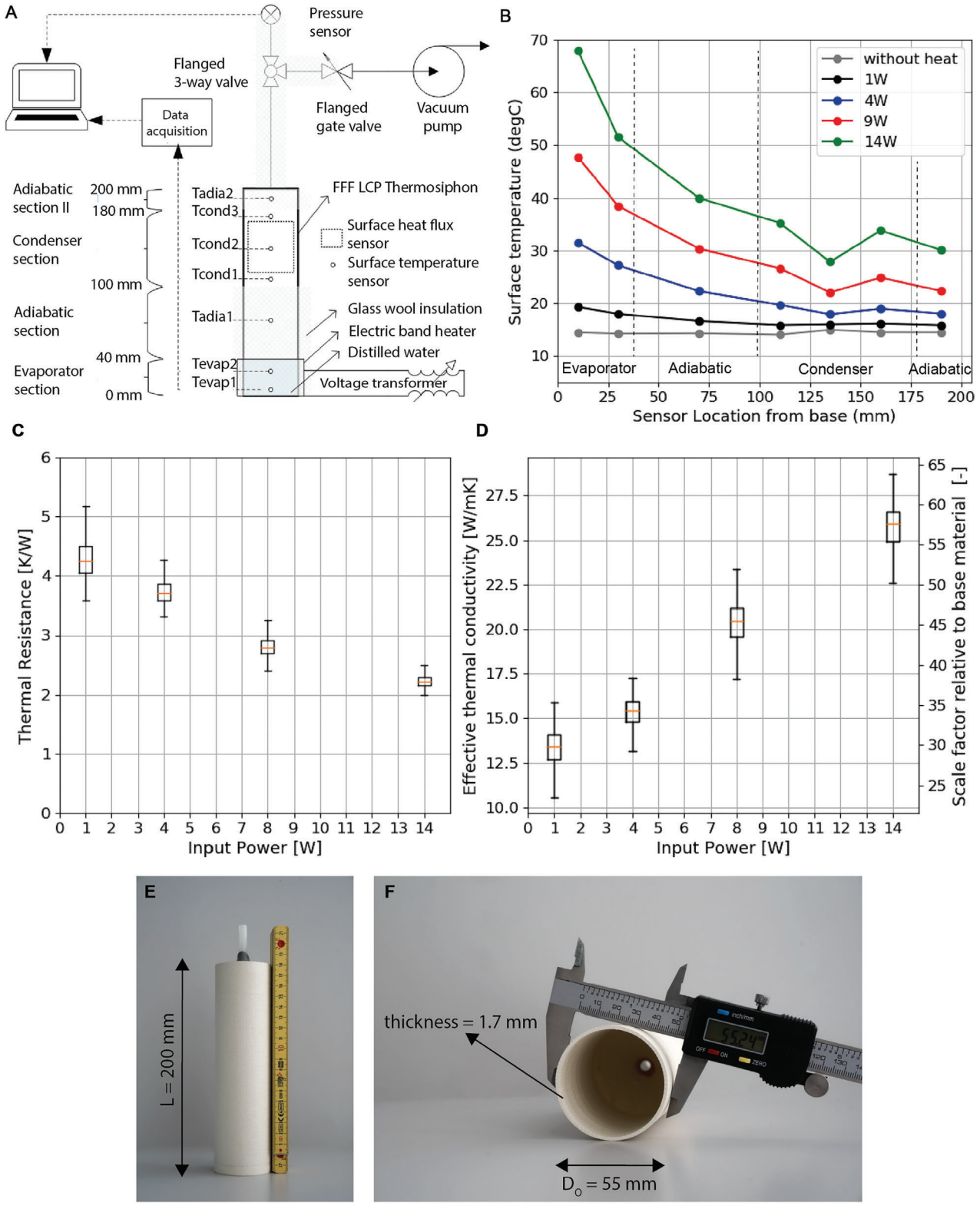

Figure 4. A) Schematic of the experimental setup to measure the thermal performance of the 3D printed LCP thermosiphon prototype consisting of equipment and measurement devices for input/output power, surface temperature and internal pressure. B) Surface temperature sensor data at the evaporator, adiabatic, and condenser sections showing measurements at steady state input power between 0 and 14 W is applied at the evaporator section. C) The thermal resistance of the prototypes for the range of input powers and D) the effective thermal conductivity values and scale factors relative to the thermal conductivity of the 3D printed LCP material. Photographs of the prototype and cross-section of the E) Photograph of the prototype and F) view inside a sliced-open prototype.

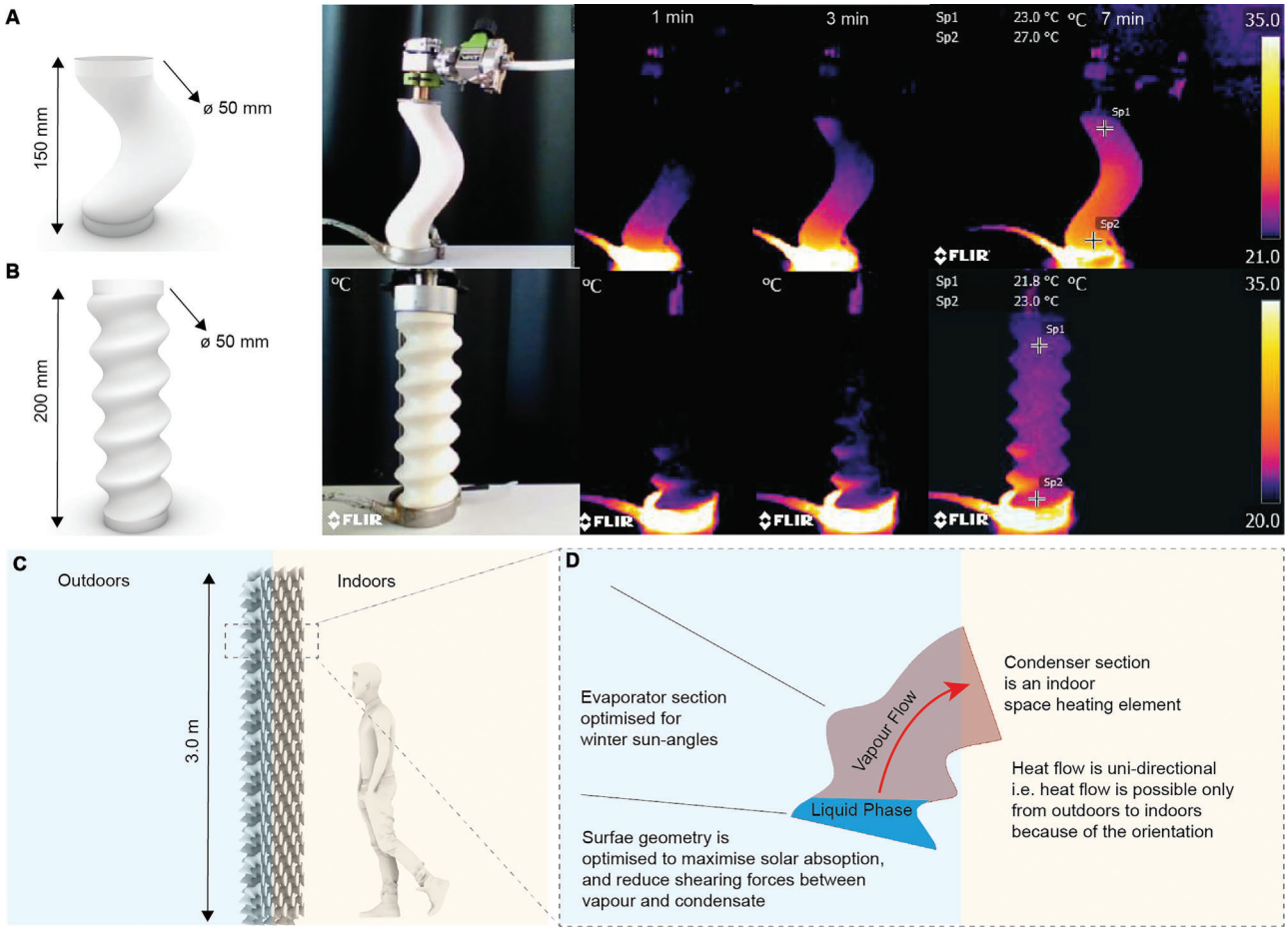

Figure 5. Thermal images of 3D printed LCP A) double-curved B) helical thermosiphons demonstrate nonlinear heat- and mass-transfer and increased surface area. The infrared (IR) images show that both geometries reach a steady state within 7 min with different surface temperature gradients. C) An application of the double curved geometry and the helical surface is shown in the selective heat-transfer façade, which D) transfers solar radiation to the inside of the building to reduce the building's heating demand. The geometry of the evaporator section is fabricated for low-winter-sun angles. The working principle of the thermosiphon ensures that heat will not be lost from the inside of the building to the outside.

The orientation of the thermosiphon ensures heat transfer works only unidirectionally. When not activated, i.e., heated, the façade would block heat loss from the inside to the outside with the thermosiphons acting as vacuum insulation. Depending on the climate zone and building typology, the application could be used for daytime heating in the winter and night-time cooling in the summer. Important aspects that will be addressed in subsequent research are the cost effectiveness of large-scale robotically extruded LCPs and recyclability of printed structures to better evaluate the potential of the application.

3.3. Summary

In this paper, we demonstrate that FFF 3D printed structures fabricated using nematically aligned liquid crystal polymers are able to withstand vacuum. Using an off-the-shelf 3D printer, we successfully fabricated single-walled (0.8–1.6 mm) LCP vacuum-tight elements without postprocessing. We identified and tested optimal FFF parameters (printing temperature 330 °C, layer height 0.1 mm, and the ratio of layer width to nozzle diameter 2.0) and used a continuous "spiral" print path to reduce the probability of defects and air leakage. The samples demonstrated lower than 10^{-6} mbar L s^{-1} leakage during the tests, which is suitable for vacuum applications. Our study further contributes to the current state of the art by demonstrating the successful fabrication of vacuum-tight LCP components using FFF, with a particular focus on thermosiphons. Using the identified parameters, we demonstrated a prototype thermosiphon functioning under vacuum pressures. The prototype thermosiphon achieves a thermal resistance of 2.23 K W^{-1}, and effective thermal conductivity of 25.68 W mK^{-1}, a 58-fold increase in the conductivity of the base material (0.45 W mK^{-1}).

To demonstrate the benefit of FFF 3D printing, we prototyped thermosiphons with more complex geometries (spiral and curved) and analyzed the thermal performance using infrared images. Adding the geometric freedom enabled by FFF, we explore the integration of thermosiphons as zero-energy heat-transfer devices through digital fabrication and assembly processes. We propose and describe an architectural/building construction application for selective heat transfer through building facades to provide heating and cooling without additional

mechanical devices. In subsequent research, we will address topics such as the cost of producing LCPs, cost comparison with conventional manufacturing processes, sustainability and recyclability, and potential obstacles to scalability. The study offers a way to integrate heating and cooling performance within 3D printed and robotically fabricated building facades to reduce Green House Gas Emissions of the building sector.

4. Experimental Section

Leak Detection: Two different approaches were used to measuring leakage rates. First, a vacuum leak detector, Pfeiffer Vacuum Smart Test HLT 550, was used to measure the relative leakage rate of a test gas (Helium) infiltrating the samples. This allowed to detect the likelihood of leakage and quantify the size and/or quantity of defects. The sample was evacuated using a vacuum pump until the system reaches a leakage rate between 10^{-8} and 10^{-9} mbar L s^{-1}. The baseline internal leakage rate was normalized to 10^{-12} mbar L s^{-1} to be able to compare the different samples before conducting the leak test. The measurements were repeated four times, each time with a new sample printed under identical conditions. Details of the setup and measurement are provided in the Supporting Information S4.

Temporal Leakage Rate Measurements: Next, temporal tests were conducted to measure the absolute leakage rates for samples with optimal 3d printing parameters. The length of the samples was increased from 100 to 200 mm to detect increase in defects/leakage rate with surface area. A pressure sensor (Pfeiffer Vacuum TPG 202, measurement accuracy 0.3%) was used to read pressure measurements at 30 s intervals. Samples were connected to the setup and evacuated for 60 min and simultaneously heated the sample to remove moisture build-up. The temporal pressure increase and absolute leakage rate for each of the samples for different printing parameters is shown in Figure 4D.

The leakage rate (mbar L s^{-1}) is defined as

$$Q = \frac{\Delta P \times V}{\Delta t} \tag{1}$$

where ΔP [mbar] is the pressure difference from time t_0 to $t_1 = t_0+\Delta t$; V [L] is the internal volume the tested sample; and Δt is the measurement interval [s].

Components are classified as leaky if Q is $>10^{-4}$ mbar L s^{-1} and tight if $<10^{-6}$ [27] within 10 and 100 mbar. Consistent with the results from the leakage test, increasing the L_W:D_N ratio decreases the leakage rate, while increasing the length of the sample has no significant effect on the leakage rate. The leakage rates shown here could also be the result of outgassing of the sample and residual moisture build-up resulting in a higher leakage rate than a completely evacuated sample. In the Supporting Information S4, the long-term (>800 h) applicability of 3D printed LCP samples by measuring the leakage behavior of a 200 mm prototype cylinder printed using the optimal print parameters and path was demonstrated.

Performance Testing of the Thermosiphon Prototype: A typical thermosiphon testing methodology was used to measure the surface temperature gradient along the prototype. Detailed information, including specifications and photographs of the apparatus, evacuation-charging methodology, pressure measurements, performance definitions, and limitations of the testing approach are included in the Supporting Information S7.

As shown in Figure 4A, the thermosiphon was connected to a vacuum pump using a series of flanged vacuum-compatible connectors. A pressure sensor and surface temperature sensors were used to study the thermal performance of the prototype. First the evaporator section was filled to a fill ratio of 1.0 with distilled water and evacuated the thermosiphon for 60 min. The evaporator section of the thermosiphon was heated using a band heater controlled by a voltage transformer. Except for the condenser section, the entire experimental apparatus and prototype with 50 mm glass wool were insulated. The condenser section was exposed to the ambient environment at 15 °C, and use an electrical fan to remove heat from the condenser section via active convection. A heat flux sensor was mounted in the condenser section to measure the heat output.

The temperature, pressure and heat flux were measured to determine the prototype's performance. The input voltage was varied from 0 to 40 V (0–14 W) and measured the performance of the thermosiphon. A good correlation was observed between input power and heat generated by the band heater. A progressively decreasing correlation between input power at the evaporator section and heat output was found for the condenser section. The steady-state surface temperatures measured at various input powers are shown in Figure 4B, and the corresponding operating pressures (Supporting Information S7).

To assess the performance of the thermosiphon, the following definitions of terminology were used

$$R = \frac{T_{\text{evap,avg}} - T_{\text{cond,avg}}}{Q_{\text{out}}} \tag{2}$$

R is the thermal resistance of the thermosiphon [K/W], $T_{\text{evap,avg}}$ is the average surface temperature in the evaporator section [K] calculated by the average of the temperature sensors in the evaporator section; $T_{\text{cond,avg}}$ is the average surface temperature in the condenser section [K] calculated by the average of the temperature sensors in the condenser section, and Q_{in} is the input electrical power [W]

$$k_{\text{eff}} = \frac{L_{\text{eff}}}{A \times R} \tag{3}$$

k_{eff} is the effective thermal conductivity of the thermosiphon [W mK^{-1}], L_{eff} is the effective length of the thermosiphon calculated using the lengths of the evaporator, adiabatic and condenser sections L_{evap}, L_{adia}, and L_{cond} [m], respectively. A is the internal cross sectional area of the thermosiphon [m^2].

Supporting Information

Supporting Information is available from the Wiley Online Library or from the author.

Acknowledgements

The authors would like to thank NematX AG (Dr. Silvan Gantenbein, Dr. Raphael Heeb, Yannick Nagel, Chiara Mascolo, and Dr. Wilhelm Woigk) for support and advice on 3d printing LCPs; Martin Kloeckner, Michael Leopold, and Sandro Tiegermann (Laboratory Support Group, ETH Zurich) for their expertise on vacuum components and testing; Oliver Fellman (Hochschule Luzern) for performing the thermal testing; Ina Cheibas for supporting with geometric modeling; Gabriel Sanchez for helping with experimental setups; Xiong Shuyan for conducting preliminary statistical modeling and testing; and Dr. Victor Petrov (Nuclear Systems and Multiphase Flows Laboratory) for advice on the performance testing of thermosiphons. The authors thanked ETH Zurich for awarding an ETH grant to support this research.

Open access funding provided by Eidgenossische Technische Hochschule Zurich.

Conflict of Interest

The authors declare no conflict of interest.

Data Availability Statement

The data that support the findings of this study are available in the Supporting Information of this article.

Keywords

3d printing, liquid crystal polymers, thermosiphons, vacuum

Received: March 14, 2023
Revised: May 23, 2023
Published online:

[1] A. Paolini, S. Kollmannsberger, E. Rank, *Addit. Manuf.* **2019**, *30*, 100894.
[2] M. Wiese, S. Thiede, C. Herrmann, *Addit. Manuf.* **2020**, *36*, 101582.
[3] J. C. Najmon, S. Raeisi, A. Tovar, in *Additive Manufacturing for the Aerospace Industry* (Eds: F. Froes, R. Boyer), Elsevier, New York **2019**, pp. 7–31. https://doi.org/10.1016/B978-0-12-814062-8.00002-9
[4] S. Catchpole-Smith, R. R. J. Sélo, A. W. Davis, I. A. Ashcroft, C. J. Tuck, A. Clare, *Addit. Manuf.* **2019**, *30*, 100846.
[5] S. Chekurov, J. Kajaste, K. Saari, H. Kauranne, M. Pietola, J. Partanen, *Prog. Addit. Manuf.* **2019**, *4*, 55.
[6] T. B. Freeman, M. A. Messenger, C. J. Troxler, K. Nawaz, R. M. Rodriguez, S. K. S. Boetcher, *Addit. Manuf.* **2021**, *39*, 101839.
[7] J. P. Kelly, L. R. Finkenauer, P. Roy, J. K. Stolaroff, D. T. Nguyen, M. S. Ross, A. T. Hoff, J. J. Haslam, *Addit. Manuf.* **2022**, *56*, 102937.
[8] J.-H. You, K. Park, *Addit. Manuf.* **2021**, *41*, 101947.
[9] Y. Y. Park, I. C. Bang, presented at Transactions of the Korean Nuclear Society Virtual spring Meeting, May **2021**.
[10] F. Belfi, F. Iorizzo, C. Galbiati, F. Lepore, *J. Heat Transfer* **2019**, *141*, 095001..
[11] M. R. Khosravani, T. Reinicke, *Appl. Mater. Today* **2020**, *20*, 100689.
[12] J. Huang, W. Zhou, J. Xiang, C. Liu, Y.u Gao, S. Li, W. Ling, *Appl. Therm. Eng.* **2020**, *175*, 115392.
[13] C. Oshman, B. Shi, C. Li, R. Yang, Y. C. Lee, G. P. Peterson, V. M. Bright, *J. Microelectromech. Syst.* **2011**, *20*, 410.
[14] G.-W. Wu, S.-L.i Chen, W.-P. Shih, *Front. Heat Pipes* **2012**, *3*, 023003.
[15] C. Yang, C. Song, W. Shang, P. Tao, T. Deng, *Prog. Nat. Sci.: Mater. Int.* **2015**, *25*, 51.
[16] K.-S. Yang, T.-Y. Yang, C.-W. Tu, C.-T. Yeh, M.-T. Lee, *Energy Convers. Manage.* **2015**, *100*, 37.
[17] G. Gamboa, S. Mazumder, N. Hnatchuk, J. A. Catalan, D. Cortes, I. Chen, P. Perez, W. Brostow, A. Kaul, *J. Vac. Sci. Technol. A* **2020**, *38*, 042201.
[18] S. Al-Hasni, G. Santori, *Vacuum* **2020**, *171*, 109017.
[19] S. Gantenbein, K. Masania, W. Woigk, J. P. W. Sesseg, T. A. Tervoort, A. R. Studart, *Nature* **2018**, *561*, 226.
[20] J. Butt, R. Bhaskar, V. Mohaghegh, *Int. J. Adv. Manuf. Technol.* **2021**, *117*, 2679.
[21] V. E. Kuznetsov, A. N. Solonin, A. Tavitov, O. Urzhumtsev, A. Vakulik, *Rapid Prototyping J.* **2019**, *26*, 107.
[22] X. Lin, P. Coates, M. Hebda, R. Wang, Y. Lu, L. Zhang, *Polym. Test.* **2020**, *90*, 106687.
[23] G. Ćwikła, C. Grabowik, K. Kalinowski, I. Paprocka, P. Ociepka, *IOP Conf. Ser.: Mater. Sci. Eng.* **2017**, *227*, 012033.
[24] Y. Wang, W.-D. Müller, A. Rumjahn, F. Schmidt, A. D. Schwitalla, *J. Mech. Behav. Biomed. Mater.* **2021**, *115*, 104250.
[25] C. Basgul, T. Yu, D. W. Macdonald, R. Siskey, M. Marcolongo, S. M. Kurtz, *J. Mech. Behav. Biomed. Mater.* **2020**, *102*, 103455.
[26] I. Ferreira, C. Melo, R. Neto, M. Machado, J. L. Alves, S. Mould, *Rapid Prototyping J.* **2020**, *26*, 1761.
[27] K. Zapfe, *CERN Doc. Server: Prepr.* **2007**. https://cds.cern.ch/record/1047068 (accessed: May 30, 2022).
[28] A. El Magri, K. El Mabrouk, S. Vaudreuil, *J. Mater. Sci.* **2021**, *56*, 14348.
[29] A. El Magri, S. Vanaei, S. Vaudreuil, *High Perform. Polym.* **2021**, *33*, 862.
[30] T. Prater, N. Werkheiser, F. Ledbetter, D. Timucin, K. Wheeler, M. Snyder, *Int. J. Adv. Manuf. Technol.* **2019**, *101*, 391.
[31] S. Jenzer, M. Alves, N. Delerue, A. Gonnin, D. Grasset, F. Letellier-Cohen, B. Mercier, E. Mistretta, C. Prevost, A. Vion, J.-P. Wilmes, *J. Phys.: Conf. Ser.* **2017**, *874*, 012097.
[32] A. Y. Dobrovskiy, V. M. Nazarychev, I. V. Volgin, S. V. Lyulin, *Membranes* **2022**, *12*, 856.
[33] F. Li, C. Zhang, Y. Weng, *ACS Omega* **2020**, *5*, 18675.
[34] J. Lin, S. Shenogin, S. Nazarenko, *Polymer* **2002**, *43*, 4733.
[35] C. D. Armstrong, N. Todd, A. T. Alsharhan, D. I. Bigio, R. D. Sochol, *Adv. Mater. Technol.* **2021**, *6*, 2000829.
[36] H. Rupp, W. H. Binder, *Adv. Mater. Technol.* **2020**, *5*, 2000509.
[37] S. G. M. Uzel, R. D. Weeks, M. Eriksson, D. Kokkinis, J. A. Lewis, *Adv. Mater. Technol.* **2022**, *7*, 2101710.
[38] A. Faghri, *Front. Heat Pipes* **2014**, *5*, https://doi.org/10.5098/fhp.5.1.
[39] R. S. Gaugler, "Heat transfer device," US2350348A, June 06, 1944. https://patents.google.com/patent/US2350348A/en (accessed: November 16, 2021).
[40] H. Jouhara, A. Chauhan, T. Nannou, S. Almahmoud, B. Delpech, L. C. Wrobel, *Energy* **2017**, *128*, 729.
[41] R. Singh, A. Akbarzadeh, M. Mochizuki, T. Nguyen, *Front. Heat Pipes* **2012**, *2*.
[42] M. S. El-Genk, H. H. Saber, *Int. J. Heat Mass Transfer* **1999**, *42*, 889.
[43] B. Fadhl, L. C. Wrobel, H. Jouhara, *Appl. Therm. Eng.* **2013**, *60*, 122.
[44] M. Mahdavi, S. Qiu, S. Tiari, *Appl. Therm. Eng.* **2015**, *81*, 325.
[45] L. L. Vasiliev, S. V. Konev, in *Advances in Heat Pipe Technology* (Ed: D. A. Reay), Pergamon, Oxford **1982**, pp. 313–325. https://doi.org/10.1016/B978-0-08-027284-9.50033-4
[46] Z. Han, C. Chang, *Polymers* **2023**, *15*, 414.
[47] B. Mohseni-Gharyehsafa, Y. V. Lyulin, S. A. Evlashin, O. A. Kabov, H. Ouerdane, *Therm. Sci. Eng. Prog.* **2022**, *28*, 101001.
[48] E. Castañeda, B. Lauret, J. M. Lirola, G. Ovando, *FDE* **2015**, *3*, 1.
[49] M. B. Mungenast, *"3D-Printed Future Facade"*, Technical University of Munich, Munich, Germany **2019**.
[50] V. Piccioni, M. Leschok, L. O. Grobe, S. Wasilewski, B. Seshadri, I. Hischier, A. Schlüter, *Adv. Mater. Technol.* **2023**, *8*, 2201200.
[51] M. Leschok, I. Cheibas, V. Piccioni, B. Seshadri, A. Schlüter, F. Gramazio, M. Kohler, B. Dillenburger, *Autom. Constr.* **2023**, *152*, 104918.
[52] D. Delgado Camacho, P. Clayton, W. J. O'brien, C. Seepersad, M. Juenger, R. Ferron, S. Salamone, *Autom. Constr.* **2018**, *89*, 110.
[53] N. Labonnote, A. Rønnquist, B. Manum, P. Rüther, *Autom. Constr.* **2016**, *72*, 347.
[54] M. Dhangar, K. Chaturvedi, M. Mili, S. S. Patel, M. A. Khan, H. N. Bhargaw, A. K. Srivastava, S. Verma, *Polym. Adv. Technol.* **2023**, *34*, 1425.
[55] B. Furet, P. Poullain, S. Garnier, *Addit. Manuf.* **2019**, *28*, 58.
[56] International Energy Agency, "Buildings", https://www.iea.org/topics/buildings (accessed: March 2021).